



Ant Colony Optimization-based method for optic cup segmentation in retinal images



Rafael Arnay*, Francisco Fumero, Jose Sigut

Department of Computer Science and Systems, University of La Laguna, Spain

ARTICLE INFO

Article history:

Received 21 October 2015

Received in revised form 3 October 2016

Accepted 19 October 2016

Available online 27 October 2016

Keywords:

Ant Colony Optimization

Optic cup segmentation

Retinal images

ABSTRACT

An accurate detection of the cup region in retinal images is necessary to obtain relevant measurements for glaucoma detection. In this work, we present an Ant Colony Optimization-based method for optic cup segmentation in retinal fundus images. The artificial agents will construct their solutions influenced by a heuristic that combines the intensity gradient of the optic disc area and the curvature of the vessels. On their own, the exploration capabilities of the agents are limited; however, by sharing the experience of the entire colony, they are capable of obtaining accurate cup segmentations, even in images with a weak or non-obvious pallor. This method has been tested with the RIM-ONE dataset, yielding an average overlapping error of 24.3% of the cup segmentation and an area under the curve (AUC) of 0.7957 using the cup to disc ratio for glaucoma assessment.

© 2016 Elsevier B.V. All rights reserved.

1. Introduction

It is estimated that 80 million people will be affected by glaucoma by the year 2020 [1]. This illness is characterized by the progressive degeneration of optic nerve fibers. Eventually, this degeneration leads to structural changes in the optic nerve head, also referred to as the “optic disk”. The vision loss occurs gradually over a long period of time; however, this disease cannot be cured and is asymptomatic in the initial stages, which makes early detection crucial for slowing down its progression.

The optic disk (OD) is the area where ganglion cell axons exit the eye to form the optic nerve, through which visual information is transmitted to the brain [2]. The OD contains two distinct regions: a central area known as the optic cup (OC), which is usually brighter than the rest of the disk, and a peripheral area known as the neuroretinal rim, where the nerve fibers bend into the cup region [8]. These structures are depicted in Fig. 1.

There are two main strategies for automatically assessing the optic nerve head [4]. The first is to extract image features and train binary classifiers to distinguish between healthy and glaucomatous patients [5,6,8]. The other strategy consists of following clinical indicators. As noted above, as the glaucoma advances, there is a loss of optic nerve fibers. This leads to structural changes in the OD. Specifically, an enlargement of the OC region and a thinning of

the neuroretinal rim. There are several parameters that are indicative of glaucoma risk factors, such as the vertical cup to disc ratio (CDR) [7], peripapillary atrophy (PPA) [8], disc diameter [9], notching [10] and the ISNT rule [11], etc. The CDR is well accepted and commonly used. A large CDR represents a higher glaucoma risk. In recent years some approaches have been proposed for performing automatic CDR-based classification using 3-D images [12–15]. The high cost of obtaining such images, however, means they are not easily available. Thus, 2-D color fundus images are still the preferred option.

This work describes a system that uses the Ant Colony Optimization (ACO) metaheuristic [16] to obtain an optic cup segmentation in 2-D fundus images. In these metaheuristics, artificial agents use some a priori knowledge of the problem to construct their solutions. In this case, the heuristic information combines the intensity gradient in the optic disc area and the curvature associated with the vessels. Though the individual exploration capabilities of the agents are limited, they can use their shared memory to construct paths in areas where there is no heuristic information, resulting in a good segmentation of the optic cup even in images with a weak or non-obvious pallor. The system has been tested in the newly created RIM-ONE database [17], yielding encouraging results.

This paper is organized as follows: Section 2 gives an overview on approaches in the field of optic cup segmentation. Section 3 provides details on the proposed method. Section 4 shows some results of the ACO-based cup segmentation on images in the RIM-ONE database and a comparison with other methods. Finally, Section 5 presents the conclusions.

* Corresponding author.

E-mail address: rafa@isaatc.ull.es (R. Arnay).

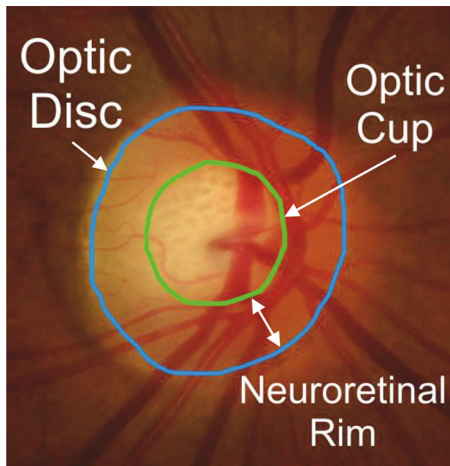


Fig. 1. Example of disc and cup segmentation.

2. Related work

Segmenting the cup from 2-D fundus images is a challenging task. When depth images are available, the segmentation process is simplified, as depth is the most discriminant indicator of the boundary of the cup [18]. Depth images are not frequently available, however. When working without depth information, two landmarks determine the cup region. The first one is the *pallor*, which is defined as the maximum color contrast inside the disc region [12]. The other clue to the presence of the cup boundary is that small vessels tend to bend as they traverse from the disc to the cup [10], [19]. Given that the features used for the cup segmentation are more subtle than those used to segment the disc, fewer methods have been developed for cup segmentation than for disc segmentation. In order to exploit the contrast variation in the pallor region, intensity thresholding has been used in [20], [21]. Joshi et al. [22] make use of cup symmetry after thresholding to obtain the cup segmentation. However, the large intensity variations in the pallor region across patients make fixed thresholding-based approaches inadequate for dealing with cup segmentation. Wong et al. [23] rely on the presence of edges in the pallor region to apply a level-set based approach. However, in many patients there is no obvious intensity transition in the pallor region that can be detected as an edge. One feature used to address the problems that arise from the use of intensity variations in the pallor region on its own is the presence of small vessel bends. Recent methods tend to exploit both clues. Some approaches look for vessel bends in the vicinity of the initial estimate of the cup region using pallor information [24,2]. These methods rely on the initial estimate to exclude vessel bends from non-cup boundary. Additionally, in [2], the presence of vessel bends in specific areas of the disc is required, which limits the robustness of this method. A recent method proposed by Cheng et al. [4] segments the cup using a superpixel-based classification. The main drawback of this method is that the classifier tends to favor medium-sized cups, underestimating the large cups and overestimating the small ones. Other recent methods use multi-modal images to segment the cup; for example, SD-OCT scans and 2D fundus images are used in [25,26]. The problem with this type of method is that they rely on devices that obtain synchronized fundus and OCT images. These devices are still expensive and not very common.

The main challenge of cup segmentation is to find the cup boundary when there is no obvious intensity change in the pallor region. In these cases, the initial pallor estimate is imprecise and the subsequent selection of relevant vessel bends tends to fail. Instead of this hierarchical approach in which the vessel bend

filtering depends on the accuracy of the cup estimate, in this paper we propose an approach that tackles both types of information at once. The method presented uses the Ant Colony Optimization metaheuristic [16] to combine pallor information and vessel curvature. The optimal solution is approximated iteratively by the multi-agent system. By making use of pheromone deposits, agents communicate with one another across different iterations to reveal the most promising paths to follow in areas where there is no obvious pallor or vessel curvature information.

3. Method

The method described in this section uses the Ant Colony Optimization meta-heuristic to obtain cup segmentation in retinal images. This meta-heuristic is based on the foraging behavior of real ants. It is known that ants have a sort of optimization system to find food cooperatively. They start by exploring their surroundings at random. If an ant finds a food source, it will leave a trace of pheromones along the path back to the colony. If other ants detect those pheromones, they tend to follow the trail instead of continuing to search randomly, returning to the colony and reinforcing the trail if they eventually find food.

The pheromone trail evaporates over time, reducing its attractive strength. In long paths that take more time to traverse, the pheromones have more time to evaporate. Short paths, by comparison, are traversed faster, and thus the pheromone density becomes higher than in longer paths. This pheromone evaporation mechanism has the advantage of avoiding convergence at locally optimal solutions. If there is no evaporation, the paths followed by the first ants would become too attractive for subsequent ants, constraining the exploration of the solution space.

The idea of the Ant Colony Optimization algorithm is to mimic this behavior with artificial agents exploring the graph representing the problem to be solved. In order to use the ACO meta-heuristic, the segmentation problem has to be mapped to an optimization problem. The different components of the ACO algorithm are described in detail in subsequent sections.

3.1. The ACO approach

The generic representation of a combinatorial optimization problem which can be solved by ACO algorithms can be formalized as follows:

- A set N of nodes n_i .
- A set L of links l_{ij} between nodes n_i and n_j .
- A set S of states $s = \langle n_i, n_j, \dots, n_k, \dots \rangle$ defined as variable length sequences of nodes.
- A state s_{fn} is a feasible neighbor of s if s_{fn} can be reached from s in one step.
- A solution is a state that meets some exit condition.

The cup segmentation problem is formalized into the optimization problem of finding the shortest path through a graph $G = \langle N, L \rangle$, where the solutions are represented as a sequence of nodes that meet some exit condition. Subsequent sections explain how the artificial agents try to approximate the optimal solution.

3.2. Starting states, final states and exploration area

The outer contour of the exploration area is defined by the contour of the disc segmentation. The inner contour of the exploration area is defined by the circle of radius r_{min} and center (x_d, y_d) , where (x_d, y_d) is the centroid of the pixels that belong to the disc region. In order to obtain the nodes of G , the pixels in the exploration area

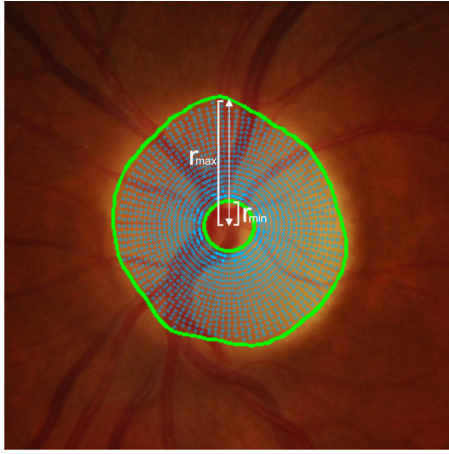


Fig. 2. Outer and inner exploration contours (green) and the pixels corresponding to the nodes of G (cyan). (For interpretation of the references to color in this figure legend, the reader is referred to the web version of the article.)

are sampled using an angular step δ_θ . Fig. 2 shows the pixels that correspond to the nodes of G .

The set of *seed points* S are the nodes where the agents begin their exploratory movements. S is the set of pixels (X_s, Y_s) , where $X_s = x_d$ and $Y_s = y_d$, with $r \in [r_{min}, r_{max}]$, where r_{max} is the radial distance from (x_d, y_d) to the disc contour at $\pi/2$.

The agents start at a seed point. They are free to explore the exploration graph G using the *Random-Proportional* motion rule (see Section 3.8). The stopping condition for an agent is triggered when it reaches a seed point again.

3.3. Heuristic function

The heuristic function is defined by some prior knowledge of the problem and characterizes the attractiveness of traversing the nodes of the exploration graph. Anatomical evidence suggests that the vessels tend to bend at the cup boundary, and that there is a gradient of intensity towards the rim area.

In order to exploit this evidence, two different methods were implemented. The first one calculates an intensity image proportional to the curvature of the vessels (Fig. 3b), while the second one obtains an intensity radial gradient of the retinal image in the disc area (Fig. 3c). Both images are combined to yield the final heuristic value for each pixel of the image.

3.3.1. Vessel curvature

Vessels are segmented from the retinal image using the method proposed in [27]. The resulting probability image is thresholded (threshold=0.15) and thinned to 1-pixel wide lines. Vessel segments are obtained by separating the lines in the bifurcations, see Fig. 3a. The curvature is calculated at every point in each segment. Given a local neighborhood of points N_c centered around point p_c , the curvature of p_c is defined as the angle $\nu \in [0, \pi]$ consisting of

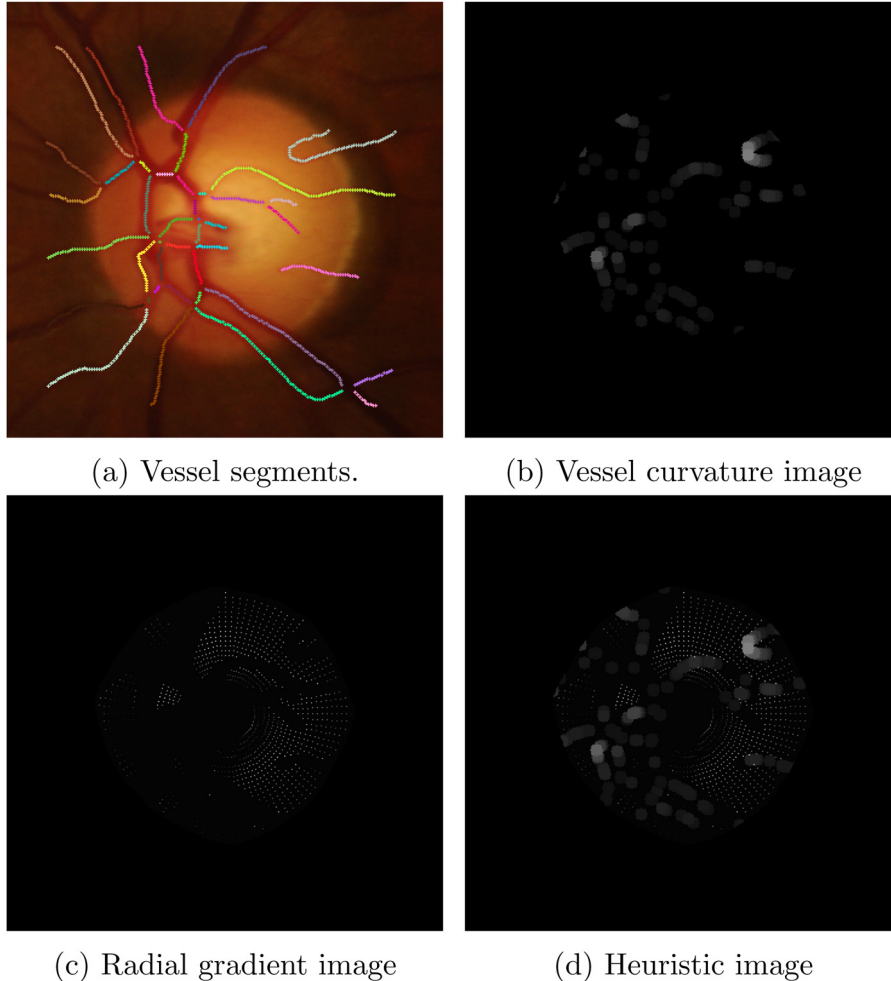


Fig. 3. The heuristic information consists of both the radial gradient and the curvature image.

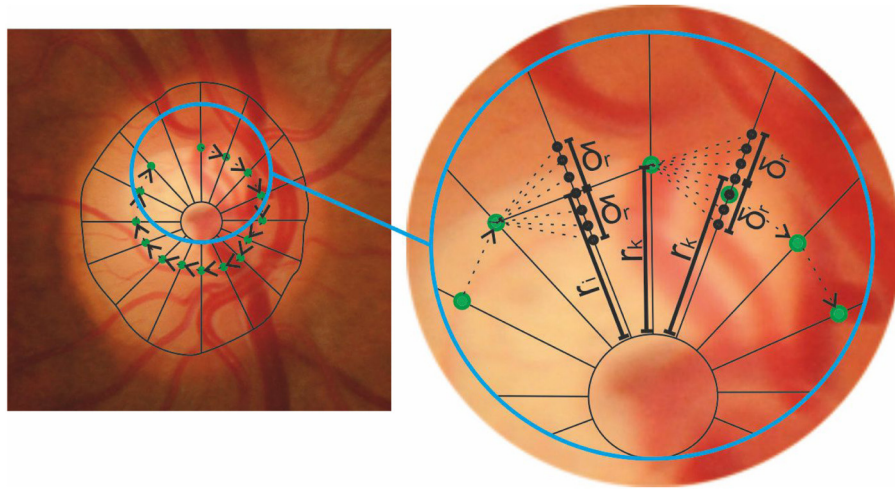


Fig. 4. Process for selecting feasible neighbors. The detailed image shows both neighbor selection processes (normal and with an attraction point, see Section 3.6).

two segments \bar{ap} and \bar{bp} , where a and b are the most distant points in the neighborhood. The intensity of each pixel in the curvature image is computed as $255 \cdot (1.0 - \nu/\pi)$, see Fig. 3b.

3.4. Radial gradient

To complement the information on vessel curvature, a radial gradient is obtained at the points of G from the green channel of the original RGB image. The radial directions of the gradient are found by incrementally adding an angular step of δ_θ . The vessels' mask is dilated and used to compute the gradient only in pixels of the disc region that do not belong to the segmented vessels. Fig. 3c shows the radial gradient image.

3.5. Reinforcing relevant vessel bends

Although vessel bends can be potential indicators of the presence of the cup boundary, they may be found in many places on the optic disc. In general, only a small subset of the vessel bends defines the cup boundary. In order to determine which vessel bends might be relevant, we select a set of reference images with associated cup segmentation ground truths. The idea is that if two retinal images share a similar pallor region, then the positions of the cup boundaries might be similar as well. Following this reasoning, relevant vessel bends in the test image could occur at positions close to the cup boundary of the reference image. During the testing phase, the incoming image is compared to the reference images to obtain a similarity measure. The similarity measure is computed as an average of the radial gradient differences per position. In order to compute the gradient differences, a mapping between the exploration graph of the test image G_{test} and the exploration graph of the reference image G_{ref} has to be defined. To do so, the relative position inside the exploration area of each node is calculated for each radial direction. This position is obtained by dividing the radius at each node by the maximum exploration range at this radial direction. We select a subset of reference images whose similarity with respect to the incoming image is above a certain threshold. We look for high curvature points in the incoming image that are close to the mapped cup boundary in the reference images. These particular vessel bends could be relevant, since they appear close to the cup boundary in a similar reference image. The intensity of the heuristic image is incremented at those points. This mechanism makes these particular vessel bends more appealing for the agents than the other vessel bends in the exploration area.

The heuristic information image is the combination of both the radial gradient and the curvature image (with the reinforced relevant vessel bends), as seen in Fig. 3d. Generally, the dilated vessel masks prevent both images from having a non-zero value at the same pixel. If this does occur, however, the value of the radial gradient is used in this position.

3.6. Feasible neighbors

The agents start at their respective seed point and construct their solutions by exploring clockwise in the disc area in steps of δ_θ . Given a point $p_k = (x_k, y_k)$, defined by $x_k = r_k \cos(\theta_k)$ and $y_k = r_k \sin(\theta_k)$, the set of feasible neighbors F_{p_k} of the agent at point p_k is a set of points defined by $X_n = R_n \cos(\theta_k + \delta_\theta)$, $Y_n = R_n \sin(\theta_k + \delta_\theta)$, where $R_n \in [r_k - \delta_r, r_k + \delta_r]$. δ_r defines the exploration range of the agents and δ_θ their angular step. These parameters control the density of the exploration paths traversed by the agents, see Fig. 4. Thus, the number of points that the agent's solution has is $2\pi/\delta_\theta$.

In order to obtain a smooth cup segmentation, the final point of the exploration paths should be close to their initial point. To achieve this, an attraction mechanism is implemented. When an agent is approaching the end of its path, the rule for selecting its feasible neighbors uses a different range as defined by $X_n = R_a \cos(\theta_k + \delta_\theta)$, $Y_n = R_a \sin(\theta_k + \delta_\theta)$, where $R_a \in [r_i - \delta_r, r_i + \delta_r]$. r_i is the distance between the center of the exploration area (x_d, y_d) and the intersection of the radius at an angle of $\theta_k + \delta_\theta$ and the segment that connects the current position of the agent and its seed point. The graph in Fig. 4 depicts the neighbor selection process.

3.7. Pheromone update

Initially, the pheromone is set to zero in every component of the exploration graph. When the agents reach a final state, they deposit an amount of pheromone in the components of the path that they have followed. The pheromone contribution is described in Eq. (1)

$$\tau_{ij}(t+1) = (1 - \rho) \cdot \tau_{ij}(t) + \rho \cdot \sum_k \Delta \tau_{ij}^k(t) \quad (1)$$

where

- agent $k \in [0, |S|]$, where $|S|$ is the number of seed points
- t is a time measure that represents the evolution of the pheromone.
- ρ is the pheromone evaporation ratio.

- $\Delta_{ij}^k(t)$ is the k -ant contribution to a state transition $s_i \rightarrow s_j$. This contribution is inversely proportional to the cost of the path traveled.

3.8. Motion rule

The motion rule is the so-called *random-proportional* rule for artificial ants [16] and determines which node, among the feasible neighbors, will be part of the next state of the agent. Each potential next state probability is defined by the parameters α and β . These parameters make it possible to fine tune the agents' behavior between heuristic information exploitation and pheromone exploitation.

$$p_{ij}^k(t) = \begin{cases} \frac{[\tau_{ij}]^\alpha [\eta_{ij}]^\beta}{\sum_{l \in Z_i^k} ([\tau_{il}]^\alpha [\eta_{il}]^\beta)}, & j \in Z_i^k \\ 0, & \text{otherwise} \end{cases} \quad (2)$$

where

- τ_{ij} is the amount of pheromone for state transition $s_i \rightarrow s_j$.
- η_{ij} is the heuristic value of state transition $s_i \rightarrow s_j$, which corresponds to the intensity of the heuristic image at the last node of s_j .
- p_{ij}^k is the probability of state transition $s_i \rightarrow s_j$.
- Z_i^k are the feasible neighbors of agent k in state s_i .

When there are neither heuristic values nor pheromone trails, the agent's next state is randomly selected from among the feasible neighbors.

3.9. Cost function

When an agent reaches the stopping condition, the cost of the path that it followed is calculated. The cost of moving towards a pixel is inversely proportional to the heuristic value at that pixel.

$$cost_{path} = \sum_{(x,y) \in path} 255 - \eta_{(x,y)} \quad (3)$$

where $\eta_{(x,y)}$ is the intensity of the heuristic image at pixel (x, y) .

3.10. Agent management

As explained in Section 3.3, this particular application of ACO uses a heuristic value that is a combination of the intensity radial gradient and the curvature of the vessels. The intensity radial gradient has higher values in the pallor region, which is where the cup boundary is supposed to be. So this part of the heuristic gives us a restricted exploration zone that is narrower than the optic disc region, but that is broad enough to allow the agents to have good exploratory capabilities while preventing them from falling in local optima. As in [28], we implemented a similar configuration of the motion rule to give more importance to the heuristic in the initial iterations to try to distribute the agents in the pallor region. The curvature part of the heuristic will force the agents to pass through relevant vessel bends, meaning they will explore the pallor region by adhering to these criteria. Eventually, in subsequent iterations, the attractiveness of the pheromone trails will make the agents converge on the final solution. In order to implement this mechanism, the agents are subdivided into groups that conduct iterative explorations. The *alpha* parameter of the random-proportional motion rule is set to zero in the first iteration and is incremented in subsequent iterations.

Each seed point S_i has an associated duration ψ_i . After each iteration, the seed points are re-arranged by the minimum solution

cost found for them. The set of seed points is divided into three subsets. In the first subset, all the seed points increase ψ by δ_ψ if $\psi < (\psi_{max} - \delta_\psi)$. In the second subset, ψ remains unchanged. In the last subset ψ is decreased by δ_ψ . If $\psi_i \leq 0$, then S_i is discarded and no more agents start in this position. This mechanism optimizes the resources of the colony, gradually forcing most of the agents to explore those areas where the most promising solutions are being found. If the agents are forced to start every iteration at seed points far away from the best solutions being found, the agents tend to converge on these paths by abruptly changing their direction in the first few steps. In other words, these agents obtain anatomically unfeasible solutions because the cup boundary does not have these abrupt variations.

Pseudo-code 1 shows the main ant management routine.

Algorithm 1. Pseudo-code for the main ant management algorithm.

Data: heuristic information

Result: minimum cost path

set pheromone deposit to zero;

for each iteration i **do**

for each ant $a \in i$ **do**

 construct path (p) of ant a ;

 calculate cost (c) of p ;

 calculate pheromone contribution of a ;

 update pheromone deposit;

end

 return minimum cost path;

end

3.11. Solution extraction

Once every agent's iterations have been executed, the best path found is used as the cup boundary segmentation. In the early stages of the exploration process, the agents explore mainly based on the heuristic information. As more iterations of agents explore, the pheromone becomes more reliable and they tend to converge on fewer paths, see Fig. 5a. The cup boundary ground-truths made by experts and present in the available datasets are usually made using an ellipse or ellipsoid. Anatomically, the reason for this is that the cup boundary tends to be smooth. Thus, in order to obtain better overlapping results with respect to the available ground-truths, we interpolated the solution-paths of the agents to an ellipse prior to calculating the overlapping error. The minimum cost path is used to interpolate an ellipse using the method proposed in [29], see Fig. 5b.

4. Experimental results

4.1. Data sets

The experiments presented in this section use the RIM-ONE [17] dataset (available online at rimone.isaac.ull.es). The database consists of 159 images collected at the Hospital Universitario de Canarias and divided by experts into two groups: one group for healthy subjects and the other group for confirmed or suspected glaucoma sufferers. The group of healthy subjects features 85 images (46 females and 39 males, 48 ± 15 years) and the other group contains 39 confirmed glaucoma cases (17 females and 22 males, 68 ± 11 years) and 35 suspected glaucoma cases (21 females and 14 males, 62 ± 12.1 years). The dataset includes disc and cup segmentations from two experts.

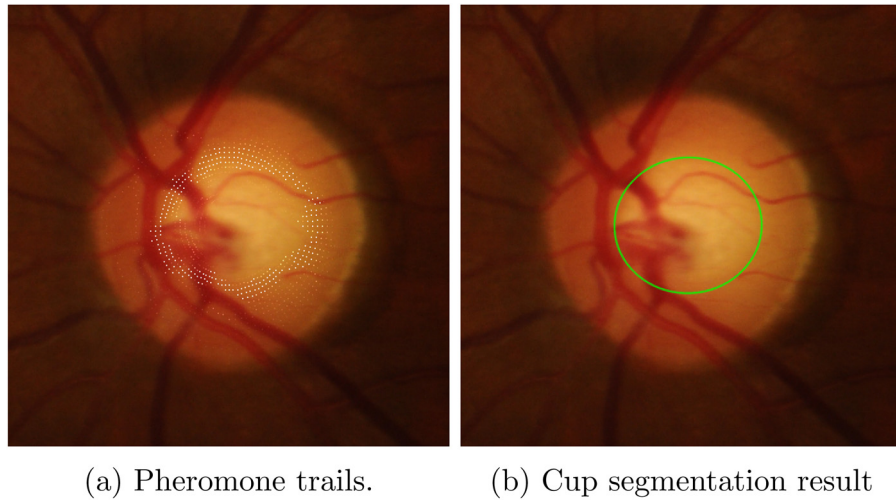


Fig. 5. Solution extraction.

As for the databases that contain ground truth of the optic disc, we have found DiaRetDB1 [30], with 89 color fundus images annotated with different diabetic retinopathies and with some elliptical optic disc segmentations, and DRIONS-DB [31], which contains 110 images and 2 ground truths of the optic disc for each one. Other examples include ARIA [32], RIM-ONE [17] and MESSIDOR [33]. ARIA only provides optic disc segmentation for some of the images.

However, optic cup ground truths are not very frequent in publicly available datasets. To the best of our knowledge, there is another public dataset with cup segmentations: the Drishti-GS [34]. It contains 101 images divided between 50 for training and 51 for testing; however, the optic cup ground truth is only available for the training images.

4.2. Optic cup segmentation

The 159 images of the RIM-ONE dataset are divided into 79 images for reference (train) (see Section 3.3) and 80 images for testing. The overlapping error is computed as the evaluation metric

$$E = 1 - \frac{\text{Area}(A \cap B)}{\text{Area}(A \cup B)} \quad (4)$$

where A and B denote the segmented and the ground truth optic cups respectively.

In order to define the exploration range of the agents, a disc segmentation is needed. Generally speaking, the optic disc segmentation is easier to obtain than the optic cup segmentation. This is because the gradient of intensity at the disc boundary is normally more evident than at the cup boundary. Although the method presented is intended to be used as a cup segmentation method, it can be used to obtain the disc segmentation by not restricting the outer exploration range of the agents and modifying the heuristic function. In this case, the heuristic only contains information about the radial gradient of the green channel image, as there is no evidence of vessels bending in the disc boundary. In order to test the validity of this method for disc segmentation, we conducted some tests in the MESSIDOR dataset, obtaining an average overlapping error of 15.25%, which is comparable with other state-of-the-art disc segmentation methods like Superpixel 12.5% [4] or CHT 14.0% [35]. We use the disc segmentation as a rough estimate of the outer exploration range of the agents in the cup segmentation process. Empirical test have shown that the disc segmentations obtained in the RIM-ONE dataset are enough to accurately represent exploration areas for the agents to detect the cup boundaries.

Table 1

Percentage of images per E interval and μ_E for cup segmentation with the proposed method using the RIM-ONE dataset.

	$E \leq 0.1$	$E \leq 0.2$	$E \leq 0.3$	$E \leq 0.4$	$E \leq 0.5$	μ_E
Expert 1	2%	27%	75%	96%	99%	24.3%
Expert 2	3%	21%	54%	92%	99%	26.3%

4.2.1. Parameter influence

There are some important parameters that have to be adjusted in order to obtain the best results with the proposed method. These parameters are: α and β , which affect the motion rule described in Section 3.8, the number of iterations, and the resolution of the exploration paths of the agents.

A set of experiments was carried out to evaluate the performance under different parameter configurations. The best configuration found was: $\alpha = 3.0$, $\beta = 3.0$, ant exploration resolution = 100, number of iterations = 250 and number of ants per iteration = 50, see Table 1.

Using the parameter configuration described above as a starting point, we have varied each parameter individually to see its influence. Some of these parameters mainly affect the quality of the solutions found, while some have more impact on the computation time needed to obtain the solutions.

α and β : these parameters affect the motion rule of the artificial agents. β determines the relative importance of heuristic exploration during the neighbor selection process. This parameter remains constant throughout the iterations. The higher its value, the faster the agents converge on high heuristic values. This may lead to a partial exploration of the solution space, resulting in sub-optimal solutions. α determines the relative importance of the pheromone trail exploration. This parameter is equal to zero in the first iteration and is then incremented proportionally to reach the desired value in the last iteration.

Table 2 shows the average overlapping error for different configurations of α and β .

Table 2

μ_E for cup segmentation with different combinations of α and β parameters.

	$\alpha = 0$	$\alpha = 1$	$\alpha = 3$	$\alpha = 5$
$\beta = 0$	27.3%	26.2%	25.1%	24.8%
$\beta = 1$	26.2%	25.7%	25.6%	25.3%
$\beta = 3$	25.5%	24.9%	24.3%	24.7%
$\beta = 5$	26.4%	26.0%	25.3%	24.9%

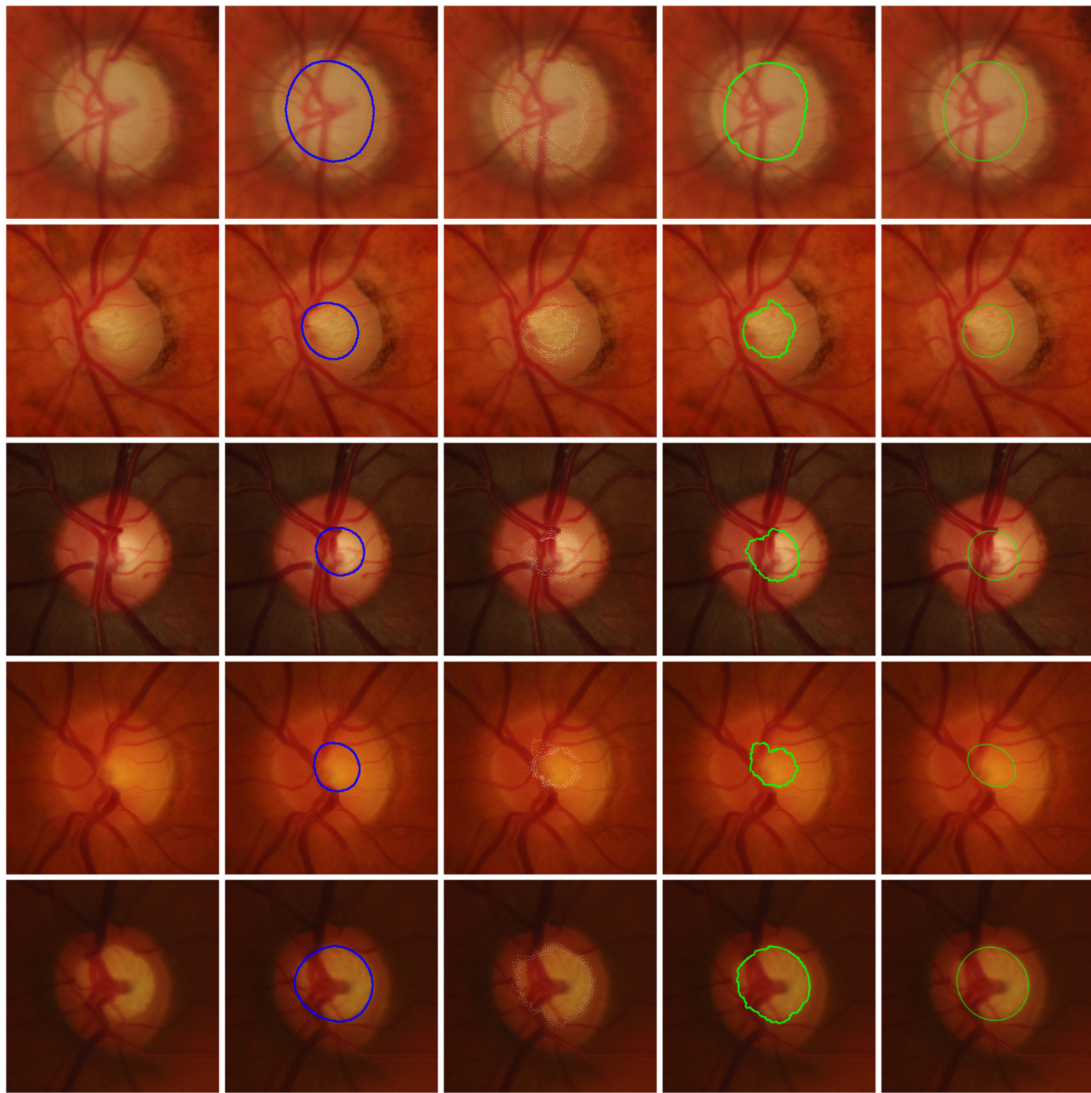


Fig. 6. Several cup segmentations with the proposed method. Sequentially depicted in each row are the original image, the ground truth segmentation, the pheromone trails in the last iteration, the solution path and the interpolated ellipse that represents the cup segmentation.

Table 3
Cup overlapping error for different path resolution parameter.

	$E \leq 0.1$	$E \leq 0.2$	$E \leq 0.3$	$E \leq 0.4$	$E \leq 0.5$	μ_E
Path res. = 20	0%	6%	14%	35%	51%	52.3%
Path res. = 50	3%	22%	63%	85%	92%	28.5%
Path res. = 100	2%	27%	75%	96%	99%	24.3%

Path resolution: this is the parameter that affects the overlapping error E the most. At lower resolutions, the paths constructed by the agents do not have enough points to accurately represent the shape of the cup boundary, see Table 3.

Number of iterations: this parameter does not affect the quality of the solutions found as much as the computation time. Table 4 gives the computation times for different numbers of iterations (Intel Core i5 2.5 GHz 8 GB RAM).

Table 4
Computation time(s) for different number of iterations (Intel Core i5 2.5 GHz 8 GB RAM).

Number of iterations	10	20	50	100	200	500	1000
Computation time (s)	0.013	0.026	0.058	0.11	0.22	0.51	0.99

Fig. 6 shows different cup segmentations. Sequentially depicted in each row are the original image, the ground truth segmentation, the pheromone trails in the last iteration, the solution path and the interpolated ellipse that represents the cup segmentation.

4.2.2. Comparison with other methods

A recent comparison of cup segmentation methods presented in [4] uses the Singapore Malay Eye Study (SiMES) dataset. This dataset contains disc and cup segmentations of 650 images, but it is not publicly available. In order to establish some sort of comparison between the ACO-based method presented and the methods compared in [4], we have conducted the same test on the RIM-ONE dataset. Table 5 shows the percentage of images per E interval and μ_E for cup segmentation using different methods in the SiMES dataset.

As we can see, the ACO-based cup segmentation method presented performs as well in the RIM-ONE dataset as the best method (Superpixel [4]) in the SiMES dataset. Among the two experts, the best overlapping error obtained with the presented ACO-based method is 24.3%. It seems that the method presented in [4] is compared to a single ground truth, yielding an overlapping error of 24.1%. Both methods make use of an equal proportion of train/test (50%) splits of the available images. We have been unable

Table 5

Percentage of images per E interval and μ_E for cup segmentation using different methods in the SiMES dataset [4].

	$E \leq 0.1$	$E \leq 0.2$	$E \leq 0.3$	$E \leq 0.4$	$E \leq 0.5$	μ_E
Thresholding [22]	0%	3%	15%	31%	47%	53.5%
R-bend [2]	0%	4%	28%	56%	77%	39.5%
ASM [36]	3%	25%	51%	76%	88%	31.3%
Regression [37]	6%	29%	62%	81%	95%	28.4%
Superpixel [4]	8%	42%	75%	90%	96%	24.1%

to establish a more accurate comparison with this method because we do not have access to either the SiMES dataset or the algorithm presented in [4]. However, it is worth noting that since retinal fundus images have considerable similarities, above a certain database size the complexity of the cup segmentation problem is similar. In this sense, the comparisons made, even using different datasets, can accurately describe the relative performance of both methods. The main drawback of the method presented in [4] is that the classifier tends to favor medium-sized cups, underestimating the large cups and overestimating the small ones. This is compensated by using a large number of training images. In the method presented, the advantage of using the similarity measure with the reference images (see Section 3.3) is that even a small proportion of small or large cups will be taken into account if they are above the similarity threshold with respect to the test images.

4.2.3. Glaucoma screening

In this section, the disc and cup segmentations obtained with the method presented in the RIM-ONE dataset are used to obtain a cup to disc ratio (CDR) using the vertical diameters in order to measure their accuracy. The CDR error is computed as:

$$\delta = |CDR_e - CDR| \quad (5)$$

where CDR_e is the manual CDR obtained by the experts. Fig. 7 shows the ROC curves for the glaucoma screening by two experts and the proposed method.

The average CDR error obtained with the proposed method is 0.077 and 0.070 for healthy and glaucomatous images respectively. The area under the curve (AUC) is 0.7957. The AUC for Experts 1 and 2 is 0.8287 and 0.8623 respectively.

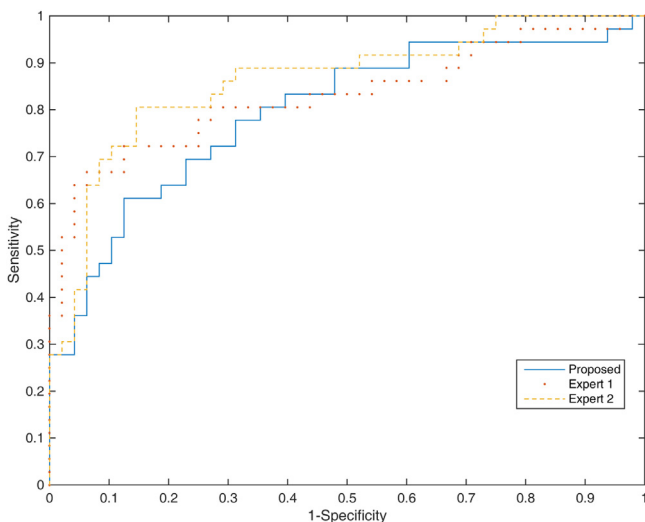


Fig. 7. ROC curves of glaucoma screening by two experts and the proposed method in the RIM-ONE [17] database.

5. Conclusion

In this paper we presented an Ant Colony Optimization-based method for optic cup segmentation in retinal fundus images. The method is based on the evolution of a colony of artificial agents that iteratively search for the best solution path. The agents are influenced by heuristic information that combines the intensity gradient in the disc area and the curvature of the vessels. There are images where the pallor is weak or non-obvious. In these cases, most cup segmentation methods exhibit difficulties. However, in the ACO-based method proposed, the agents can use their shared memory (pheromone trails) to construct feasible solutions even where there is a lack of heuristic information, obtaining good enough cup segmentation results in difficult images. The method has been tested using the RIM-ONE dataset and compared to other state-of-the-art methods. Experimental results show a best average overlapping error of 24.3% in the RIM-ONE dataset, which is equivalent to the best method reported so far for the SiMES dataset. Also, the proposed method has been used to derive the cup-to-disc ratio for the glaucoma assessment. ROC curves comparing the method with assessments from two different experts show promising results. The Area Under the Curve (AUC) for the proposed method is 0.7957, while the AUCs for the two experts are 0.8287 and 0.8623. To the best of our knowledge, no previous cup segmentation results have been published using the RIM-ONE dataset. In this sense, this could be a good starting point to establish a comparison of cup segmentation methods using a public dataset.

Acknowledgements

This research has been supported by a grant from the Spanish Government (AP2012-6800) and by Project PI12/02301 of the Fondo de Investigación Sanitaria, Instituto Carlos III (co-financed with Feder funds).

References

- [1] H. Quigley, A. Broman, The number of people with glaucoma worldwide in 2010 and 2020, *Br. J. Ophthalmol.* 90 (3) (2006) 262–267.
- [2] G. Joshi, J. Sivaswamy, S. Krishnadas, Optic disk and cup segmentation from monocular color retinal images for glaucoma assessment, *IEEE Trans. Med. Imaging* 30 (6) (2011) 1192–1205.
- [3] R. Bock, J. Meier, L. Nyl, J. Hornegger, G. Michelson, Glaucoma risk index: automated glaucoma detection from color fundus images, *Med. Image Anal.* 14 (3) (2010) 471–481.
- [4] J. Cheng, J. Liu, Y. Xu, F. Yin, D. Wong, N.-M. Tan, D. Tao, C.-Y. Cheng, T. Aung, T. Wong, Superpixel classification based optic disc and optic cup segmentation for glaucoma screening, *IEEE Trans. Med. Imaging* 32 (6) (2013) 1019–1032.
- [5] J. Meier, R. Bock, G. Michelson, L. Nyl, J. Hornegger, Effects of preprocessing eye fundus images on appearance based glaucoma classification *Lecture Notes in Computer Science (including subseries Lecture Notes in Artificial Intelligence and Lecture Notes in Bioinformatics)* 4673 LNCS, 2007, pp. 165–172.
- [6] R. Bock, J. Meier, G. Michelson, L. Nyl, J. Hornegger, Classifying glaucoma with image-based features from fundus photographs *Lecture Notes in Computer Science (including subseries Lecture Notes in Artificial Intelligence and Lecture Notes in Bioinformatics)* 4713 LNCS, 2007, pp. 355–364.
- [7] T. Damms, F. Dannheim, Sensitivity and specificity of optic disc parameters in chronic glaucoma, *Investig. Ophthalmol. Vis. Sci.* 34 (7) (1993) 2246–2250.
- [8] J. Jonas, M. Fernandez, G. Naumann, Glaucomatous parapapillary atrophy: occurrence and correlations, *Arch. Ophthalmol.* 110 (2) (1992) 214–222.
- [9] M.O.d. Hancox, Optic disc size, an important consideration in the glaucoma evaluation, *Clin. Eye Vis. Care* 11 (2) (1999) 59–62.
- [10] , in: Shields' textbook of glaucoma, 6th ed., *Clin. Exp. Optim.* 95 (2) (2012) 250, <http://dx.doi.org/10.1111/j.1444-0938.2011.00697.x>.
- [11] N. Harizman, C. Oliveira, A. Chiang, C. Tello, M. Marmor, R. Ritch, J. Liebmann, in: The ISNT rule and differentiation of normal from glaucomatous eyes, *Arch. Ophthalmol.* 124 (11) (2006) 1579–1583.
- [12] J. Xu, O. Chutatape, E. Sung, C. Zheng, P. Chew Tec Kuan, in: Optic disk feature extraction via modified deformable model technique for glaucoma analysis, *Pattern Recognit.* 40 (7) (2007) 2063–2076.
- [13] M.D. Abramoff, W.L. Alward, E.C. Greenlee, L. Shuba, C.Y. Kim, J.H. Fingert, Y.H. Kwon, in: Automated segmentation of the optic nerve head from stereo color photographs using physiologically plausible feature detectors, *Investig. Ophthalmol. Vis. Sci.* 48 (4) (2007) 1665.

- [14] Z. Hu, M.D. Abramoff, Y.H. Kwon, K. Lee, M.K. Garvin, in: Automated segmentation of neural canal opening and optic cup in 3d spectral optical coherence tomography volumes of the optic nerve head, *Investig. Ophthalmol. Vis. Sci.* 51 (11) (2010) 5708.
- [15] M. Abramoff, K. Lee, M. Niemeijer, W. Alward, E. Greenlee, M. Garvin, M. Sonka, Y. Kwon, in: Automated segmentation of the cup and rim from spectral domain OCT of the optic nerve head, *Investig. Ophthalmol. Vis. Sci.* 50 (12) (2009) 5778–5784.
- [16] M. Dorigo, C. Blum, in: Ant colony optimization theory: a survey, *Theor. Comput. Sci.* 344 (2–3) (2005) 243–278.
- [17] F. Fumero, J. Sigut, S. Alayon, M. Gonzalez-Hernandez, M. Gonzalez de la Rosa, Interactive tool and database for optic disc and cup segmentation of stereo and monocular retinal fundus images, in: *Short Papers Proceedings – WSCG* 2015, 2015, pp. 91–97.
- [18] G. Joshi, J. Sivaswamy, S. Krishnadas, in: Depth discontinuity-based cup segmentation from multiview color retinal images, *IEEE Trans. Biomed. Eng.* 59 (6) (2012) 1523–1531.
- [19] J. Jonas, W. Budde, S. Panda-Jonas, in: Ophthalmoscopic evaluation of the optic nerve head, *Surv. Ophthalmol.* 43 (4) (1999) 293–320.
- [20] K. Stapor, A. Switonski, R. Chrastek, G. Michelson, Segmentation of fundus eye images using methods of mathematical morphology for glaucoma diagnosis *Lecture Notes in Computer Science (including subseries Lecture Notes in Artificial Intelligence and Lecture Notes in Bioinformatics)*, 3039, 2004, pp. 41–48.
- [21] N. Inoue, K. Yanashima, K. Magatani, T. Kurihara, Development of a Simple diagnostic Method for the Glaucoma Using Ocular Fundus Pictures, vol. 7, 2005, pp. 3355–3358.
- [22] G. Joshi, J. Sivaswamy, K. Karan, S. Krishnadas, Optic Disk and Cup Boundary Detection Using Regional Information, 2010, pp. 948–951.
- [23] D. Wong, J. Liu, J. Lim, X. Jia, F. Yin, H. Li, T. Wong, Level-set Based Automatic Cup-to-Disc Ratio Determination Using Retinal Fundus Images in *Argali*, 2008, pp. 2266–2269.
- [24] D. Wong, J. Liu, J. Lim, H. Li, T. Wong, Automated Detection of Kinks from Blood Vessels for Optic Cup Segmentation in Retinal Images, vol. 7260, 2009.
- [25] M. Miri, M. Abramoff, K. Lee, M. Niemeijer, J.-K. Wang, Y. Kwon, M. Garvin, in: Multimodal segmentation of optic disc and cup from SD-OCT and color fundus photographs using a machine-learning graph-based approach, *IEEE Trans. Med. Imaging* (99) (2015) 1–1.
- [26] J. Bai, M. Miri, Y. Liu, P. Saha, M. Garvin, X. Wu, Graph-based optimal multi-surface segmentation with a star-shaped prior: application to the segmentation of the optic disc and cup, in: *2014 IEEE 11th International Symposium on Biomedical Imaging (ISBI)*, 2014, pp. 525–528.
- [27] A. Frangi, W. Niessen, K. Vincken, M. Viergever, Multiscale vessel enhancement filtering, in: W. Wells, A. Colchester, S. Delp (Eds.), *Medical Image Computing and Computer-Assisted Intervention – MICCAI'98*, Vol. 1496 of *Lecture Notes in Computer Science*, Springer, Berlin/Heidelberg, 1998, pp. 130–137.
- [28] A. Broggi, S. Cattani, in: An agent based evolutionary approach to path detection for off-road vehicle guidance, *Pattern Recognit. Lett.* 27 (11) (2006) 1164–1173.
- [29] J. Cheng, J. Liu, D. Wong, F. Yin, C. Cheung, M. Baskaran, T. Aung, T.Y. Wong, Automatic optic disc segmentation with peripapillary atrophy elimination, in: *Engineering in Medicine and Biology Society, EMBC, 2011 Annual International Conference of the IEEE*, 2011, pp. 6224–6227, <http://dx.doi.org/10.1109/IEMBS.2011.6091537>.
- [30] V. Kalesnykiene, J.K. Kamarainen, R. Voutilainen, J. Pietil, H. Kiviinen, H. Uusitalo, DIARETDB1 diabetic retinopathy database and evaluation protocol, 2007.
- [31] E.J. Carmona, M. Rincón, J. García-Feijó, J.M. Martínez-de-la Casa, in: Identification of the optic nerve head with genetic algorithms, *Artif. Intell. Med.* 43 (3) (2008) 243–259.
- [32] Y. Zheng, M.H.A. Hijazi, F. Coenen, in: Automated disease/no disease grading of age-related macular degeneration by an image mining approach, *Invest. Ophthalmol. Vis. Sci.* (2012).
- [33] Techno-vision, p., méthodes d'évaluation de systèmes de segmentation et d'indexation dédiées à l'ophtalmologie rétinienne. <http://messidor.crihan.fr/Techno-Vision>.
- [34] J. Sivaswamy, S. Krishnadas, G. Datt Joshi, M. Jain, A. Ujjwaft Syed Tabish, Drishti-GS: retinal image dataset for optic nerve head (ONH) segmentation, in: *2014 IEEE 11th International Symposium on Biomedical Imaging (ISBI)*, 2014, pp. 53–56.
- [35] A. Aquino, M. Gegundez-Arias, D. Marin, in: Detecting the optic disc boundary in digital fundus images using morphological, edge detection, and feature extraction techniques, *IEEE Trans. Med. Imaging* 29 (11) (2010) 1860–1869.
- [36] F. Yin, J. Liu, S.H. Ong, Y. Sun, D. Wong, N.M. Tan, C. Cheung, M. Baskaran, T. Aung, T.Y. Wong, Model-based optic nerve head segmentation on retinal fundus images, in: *Engineering in Medicine and Biology Society, EMBC, 2011 Annual International Conference of the IEEE*, 2011, pp. 2626–2629.
- [37] Y. Xu, D. Xu, S. Lin, J. Liu, J. Cheng, C.Y. Cheung, T. Aung, T.Y. Wong, Sliding window and regression based cup detection in digital fundus images for glaucoma diagnosis, in: *Medical Image Computing and Computer-Assisted Intervention-MICCAI 2011*, Springer, 2011, pp. 1–8.